ELSEVIER

Mathematics and Computers in Simulation 62 (2003) 11–20

MATHEMATICS AND COMPUTERS IN SIMULATION

www.elsevier.com/locate/matcom

Analysis of coupled oceanographic and acoustic soliton simulations in the Yellow Sea: a search for soliton-induced resonances

S.A. Chin-Bing [a,*], A. Warn-Varnas [a], D.B. King [a], K.G. Lamb [b], M. Teixeira [c], J.A. Hawkins [d]

[a] *Naval Research Laboratory, Acoustics Division, Code 7180, Stennis Space Center, Mississippi, MS 39529-5004, USA*

[b] *University of Waterloo, Waterloo, Ont., Canada N2L 3G1*

[c] *University of Puerto Rico, San Juan 00936, Puerto Rico*

[d] *Planning System Inc., Slidell, LA 70458, USA*

Abstract

The area south of the Shandong peninsula has been of great interest to both oceanographers and underwater acousticians due to the measurements of Zhou et al. [J. Acoust. Soc. Am. 90 (1991) 2042]. Over a period of years, in the summer, they observed anomalous losses in shallow water acoustic signals. They attributed the losses to acoustic mode conversions produced by solitary internal waves (solitons). Their hypothesis remains unsubstantiated due to a scarcity of oceanographic measurements in this area. In this simulation study the non-hydrostatic, 2.5-dimensional Lamb model was used to generate solitons in an adjacent, deeper area than that examined by Zhou et al. [J. Acoust. Soc. Am. 90 (1991) 2042]. Topographic variations and semi-diurnal tidal strength magnitudes were obtained from digital atlases and published data. For summer conditions, the Lamb model simulations showed that the existing semi-diurnal tidal flow over the topographic variations could lead to the formulation of internal bores and solitons. SAR observations of solitons near this region were used to select parameters and initialize the Lamb model. The resulting soliton simulations were comparable to the two-dimensional surface spectra seen in the SAR data. Soliton amplitudes of 2–7 m were indicated. Acoustic studies were made using the highly accurate finite element parabolic equation (FEPE) acoustic model applied to the initial soliton state data generated by the Lamb model. Mode decomposition of the acoustic fields in the deeper region showed that the mode conversions necessary for anomalous signal losses were present. These findings are consistent with the soliton hypothesis made by Zhou et al. [J. Acoust. Soc. Am. 90 (1991) 2042].

Keywords: Solitons; Resonances; Anomalous signal loss

* Corresponding author. Tel.: +1-228-688-4798; fax: +1-228-688-5049.
E-mail addresses: chinbing@nrlssc.navy.mil, chin-bing@ieee.org (S.A. Chin-Bing).

0378-4754/02/$ – see front matter © 2002 Published by Elsevier Science B.V. on behalf of IMACS.
PII: S0378-4754(02)00192-1

1. Introduction

Sea floor protrusions can combine with tidal flow to produce substantial upwelling of water mass that create nonlinear effects (internal waves) below the sea surface. In the shallow water ocean regions the sound speeds can have large gradients near the sea surface defining a *thermocline* region. Under such conditions internal waves take on soliton characteristics, producing a near-surface "ripple" that travels along the thermocline for very long distances (up to 100 nm). Similar conditions are also found near straits.

Solitons with large amplitudes potentially can have a significant effect on ocean acoustic propagation in shallow water regions [1–10]. Acoustic mode conversions occur due to acoustic interactions with the soliton packets. Under the right environmental conditions a large loss in acoustic signal transmission can result. This anomalous signal loss is due to the acoustic mode conversions combined with mode attenuations in the ocean bottom that are significantly larger for the converted modes. The loss occurs within a narrow band of acoustic frequencies. The anomalous loss is most prominent when there is strong coupling between the lower-order (water-borne) propagation modes and the higher-order, very lossy (bottom interacting) modes. The entire effect represents a "resonance" effect that occurs at and near the resonance frequency [11].

A decade has passed since the seminal paper on anomalous signal loss due to solitons [1]. A number of ocean acoustic experiments in other regions have shown that shallow water solitons can degrade ocean acoustic signals. However, signal losses on the order of those reported by Zhou et al. [1] have not been observed. Furthermore, it has been suggested that scattering from fish swim bladders could produce similar losses in signal, and that certain species of fish tend to seasonally congregate in dense schools. Thus, the reason for the large anomalous signal loss remains unresolved. In lieu of simultaneous collocated oceanographic and acoustic data from the Yellow Sea, we have generated our own synthetic oceanographic and acoustic data using computer simulations. Decomposition of the resulting acoustic field structure indicates that the anomalous signal loss due to large solitons hypothesis is indeed a valid explanation for the observations made by Zhou et al. [1].

2. Soliton simulations in the Yellow Sea

The purpose of this work was to determine if solitons could be the reason for the large signal loss observed by Zhou et al. [1]. No oceanographic measurements were made during their ocean acoustic experiments. Therefore, no solitons were observed. We attempted to resolve the issue by performing large scale computer simulations of the dynamic oceanography coupled with accurate ocean acoustic transmission predictions. Such an endeavor required a number of resources, including a nonlinear nonhydrostatic oceanography model and an accurate ocean acoustics propagation model.

2.1. Nonhydrostatic oceanographic model

The Lamb model [12] was used to generate computer simulations of dynamic solitons in the region around the Shandong peninsula in the Yellow Sea (Fig. 1). The model was originally created by Lamb to study the generation of internal gravity waves by tidal flow over ocean bottom topography (e.g. shelf-breaks, bank edges, and fjord sills). The model solves the fully nonlinear, nonhydrostatic Boussinesq

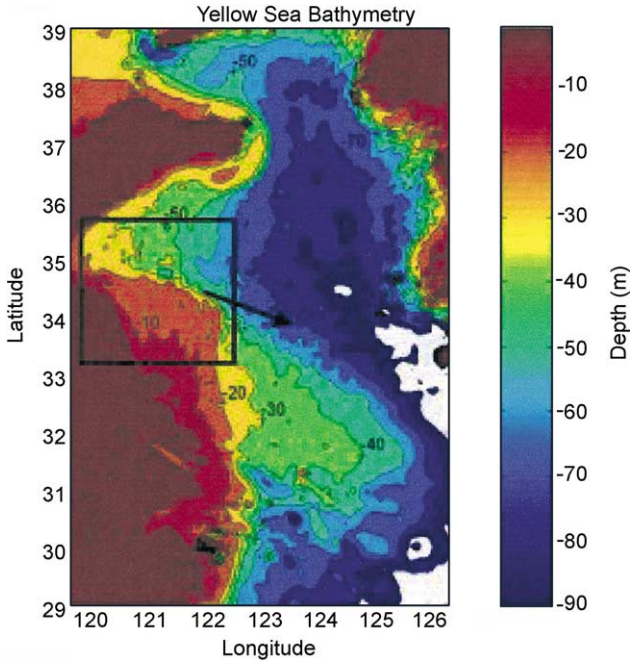

Fig. 1. Topographical map showing the Shandong peninsula region and the region (boxed area) where solitons were generated using the Lamb model. The straight line extending from the region was the track where these soliton simulations were made.

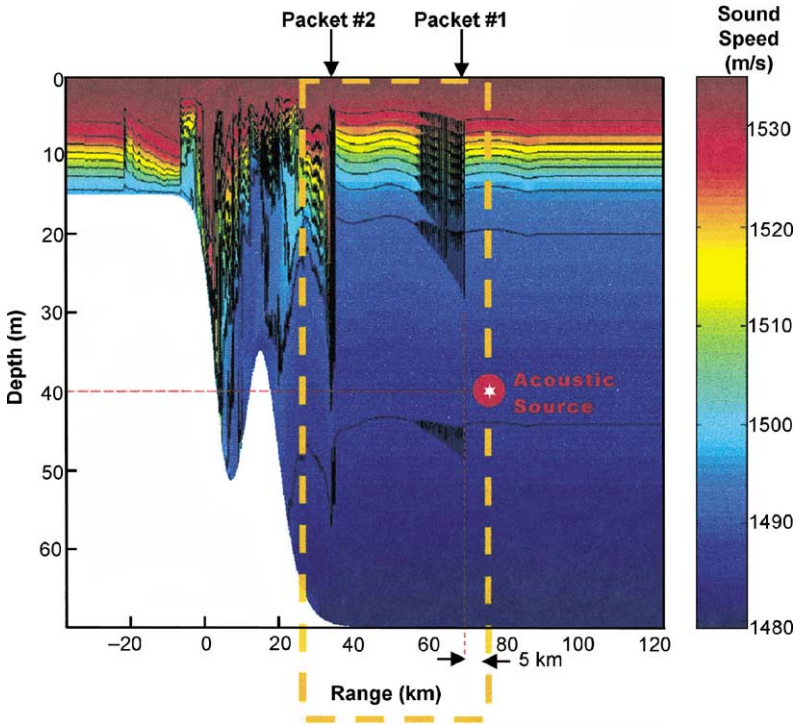

Fig. 2. A computer simulation from the Lamb model is shown. Two soliton packets are traveling along the track indicated in Fig. 1. The broken line rectangle is the ocean region where the acoustic simulations were made.

equations with Coriolis forces. It is two-dimensional with spatial variation in the vertical and cross-bank directions only; the along-bank velocity is included but does not vary in the *y*-direction, hence the designation of 2.5-dimensional. Model forcings are based on observations and measurements, in this case by the tidal flow around the Shandong peninsula. Horizontal uniform stratification is used and no frictional effects are included. The model is sensitive to topographic slope, tidal current strength, and stratification. Appendix A gives a brief discussion of the Lamb model.

2.2. Initiation of the lamb model

Model forcings were obtained from historical, measured data taken in the Shandong peninsula region. Topographic variations were obtained from a digital atlas of the region, and semi-diurnal tidal strength magnitudes were obtained from published records. For summer conditions (i.e. density variability for August), computer simulations from the Lamb model showed that the existing semi-diurnal tidal flow over the topographic variations could lead to the formulation of internal bores and solitons. Small but valid variations in the forcings parameters that initiated the Lamb model produced three slightly different soliton packets; an initial state that was valid over shorter ranges, and two distinct dynamical states, each of which were valid over very long ranges. The validity of the soliton packets was established by comparisons with SAR satellite data taken in the region. Validations of the model results are discussed in Section 2.3. The results reported here used the initial soliton state simulations. Acoustical analysis of the two dynamical soliton states is underway, with no results yet available.

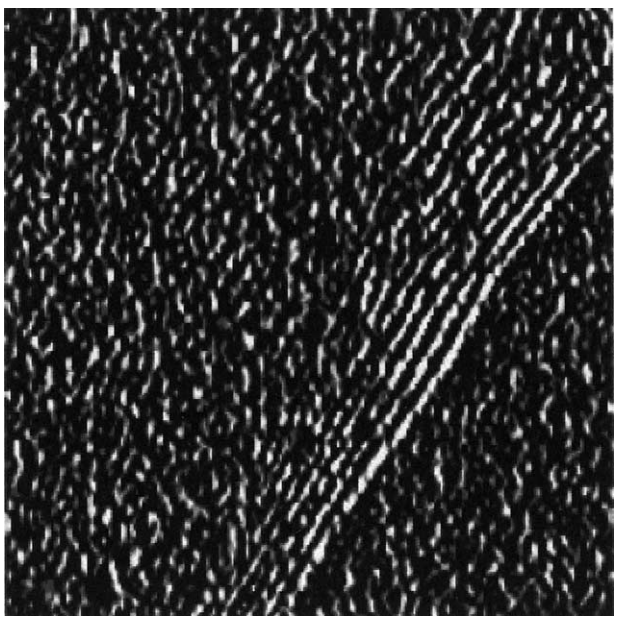

Fig. 3. Satellite photograph of soliton packets traveling away from the Shandong peninsula. The region shown is approximately the same as shown in Fig. 1 and the direction of flow is along the track indicated in Fig. 1.

2.3. Model validation using SAR images of the Yellow Sea

Soliton simulations generated by the Lamb model were benchmarked against satellite imagery observations, shown in Figs. 2 and 3. The Lamb model was initiated by tidal flow, such that it produced solitons with wave heights and spacings (i.e. wavelengths) that were very similar to those observed by SAR satellite observations (date: 22 August 1998; time: 09:42:25; orbit number: 14604; Satellite ID: Radarsat-1; processing site: Alaska SAR facility; size: 57,344 Kb; beam mode: scansar wide, 500 km × 500 km; beam position: SWB; product type: Geocoded; ascending/descending: ascending; pixel spacing: 100.00 m; northern-most latitude: 36.1379; southern-most latitude: 31.0537; western-most longitude: 121.2180; eastern-most longitude: 127.0343). As noted in Section 2.2, the SAR images were very useful in establishing the validity of the soliton simulations produced by the Lamb model, but the SAR images were not sufficient to identify a unique soliton state. Hence, in this study three slightly different soliton states were validated. We have characterized these states as the initial state and two dynamical states.

3. Acoustic model simulations

The acoustic simulations and analysis were made in the ocean environment indicated by the broken-line rectangular box shown in Fig. 2. This area contained two of the soliton wave packets that were generated by the Lamb model. All environmental inputs used in the acoustic model were consistent with those used in the Lamb model. The simulated acoustic source was placed below the thermocline (depth = 40 m, range = 80 km), such that it is downrange by 5 km from soliton packet number 1 shown in Fig. 2. The model analysis of the acoustic fields were made after they had propagated partially through soliton packet number 2, and just before the beginning of upslope propagation. The mode analysis region is indicated by the left-hand-side of the box in Fig. 2.

The finite element parabolic equation (FEPE) model [13–16] was used to predict the interactions of the acoustic fields as they propagated through the soliton packets. This model was chosen because of its documented accuracy in rang-varying ocean environments. The FEPE model contains improved energy conservation techniques and numerically stable algorithms [13,16]. Its acoustic field predictions are considered benchmark accurate. Such accuracy was required in determining the magnitude of acoustic mode conversions resulting from soliton interactions. A brief discussion of the FEPE model is given in Appendix B.

4. Analysis of the acoustic field structure

Color contour plots of the acoustic field predictions are shown in Fig. 4 for acoustic frequencies of 450, 500, and 550 Hz. The color scale represents the acoustic transmission loss, in decibels (dB), where red is the lowest loss shown (at 50 dB) and blue is the highest loss shown (at 100 dB), i.e. red indicates the strongest acoustic field and blue indicates the weakest acoustic field. The acoustic fields shown in the Fig. 4(a)–(c) are the acoustic fields that propagated within the ocean region indicated by the broken-line rectangular box shown in Fig. 2 note that the direction of acoustic propagation is reversed, i.e. the fields propagate right-to-left in Fig. 2, and left-to-right in Fig. 4. The acoustic source was located at

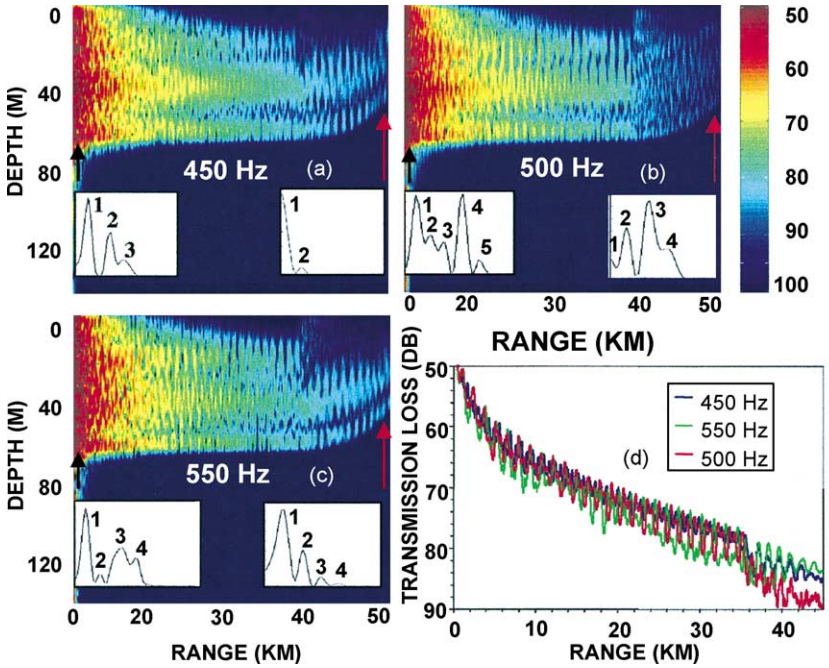

Fig. 4. Wavenumber decomposition of the vertical acoustic pressure fields before (black arrow) and after (red arrow) passing through the two soliton packets. The colored arrows indicate the location in range where the vertical pressure fields were sampled. The peaks in the wavenumber plots are indicative of the normal modes present and their relative strengths. The three figures, (a)–(c), illustrate the acoustic fields around the resonance frequency: (a) before resonance, at 450 Hz, (b) at resonance, 500 Hz, and (c) after resonance, 550 Hz. Figure (d) shows the acoustic signal loss due to the solitons when the acoustic source is at the resonance frequency.

depth = 40 m, range = 0 km. In Fig. 4(d) the acoustic receiver was located at depth = 40 m throughout the 0–50 km range.

The two inserted white graphs in each of the three contour plots, Fig. 4(a)–(c), show the vertical acoustic field structure, in wavenumbers, at the ranges indicated by the colored vertical arrows. Thus, the inserted white graph on the left-hand-side of each contour plot shows the vertical field structure of the acoustic field just after it has left the acoustic source and before it has interacted with the first soliton packet; the inserted white graph on the right-hand-side of each contour plot shows the vertical field structure of the acoustic field after it has interacted with and propagated through both soliton packets.

Of special interest are the stronger acoustic modes before and after the interactions with the soliton packets. In Fig. 4(a) acoustic mode 1 has the majority of the acoustic energy, initially, and mode 1 still has the majority of the energy after the acoustic interactions with both soliton packets. Therefore, at 450 Hz the predominate energy carrying mode does not undergo mode conversion when it interacts with the soliton packets. The intensities of modes 2 and 3 are reduced by interactions with the soliton and the ocean bottom, but their relative strengths remain unchanged and there is no evidence of mode conversion. A similar conclusion is drawn from the acoustic mode analysis shown in Fig. 4(c) where the acoustic frequency was 550 Hz. The change in relative strengths between modes 2, 3, and 4 could be due to either

mode conversions and/or different ocean bottom attenuations for the different modes. Regardless, the predominate mode 1 is unaffected.

At 500 Hz the acoustic mode analysis shown in Fig. 4(b) indicates that, initially modes 1 and 4 are predominately the strongest; but, after interacting with the soliton packets they have lost most of their acoustic energy to modes 3 and 4. This is similar to the mode conversions that Zhou et al. hypothesized. In our simulations the resonance frequency is in a narrow band, located between 450 and 550 Hz, with center resonance frequency near 500 Hz. The acoustic transmission loss curves shown in Fig. 4(d) indicate how the acoustic fields are affected by solitons when the acoustic source is near or at the resonance frequency. In this simulation when the source frequency is at the resonance frequency of 500 Hz, the loss in signal after passing through both soliton packets is approximately 5 dB more than it is at the non-resonance frequencies (e.g. 450 or 550 Hz).

These results are preliminary and no attempt has been made to propagate the converted acoustic fields further and examine the influence that ocean bottom attenuation has on the acoustic intensities at long ranges from the soliton packets. At longer ranges, if modes 2 and 3 have significantly higher mode attenuations in the ocean bottom than do modes 1 and 4, a larger loss in acoustic intensity will result from these mode conversions, and the large anomalous signal loss observed by Zhou et al. [1] is possible. If modes 1 through 4 have nearly the same magnitudes in their ocean bottom attenuations, then almost no loss in intensity will result other than what is shown in Fig. 4(d); although the acoustic interactions with the soliton packets produced mode conversions, the total acoustic pressure, which is summed over all modes, would be unchanged.

5. Summary

The simulation capabilities of a primitive equation nonlinear ocean soliton model—benchmarked against satellite observations—and a high-fidelity linear ocean acoustic propagation model have been combined to examine the hypothesis that anomalous signal losses observed in the Yellow Sea were due to a soliton resonance effect. The simulation studies presented in this paper tend to substantiate the soliton resonance hypothesis, although the simulations were made for an ocean region adjacent to the region where the anomalous signal losses were observed. Furthermore, the soliton simulations presented here represented solitons in their initial (creation) state. This initial state can be transitory, evolving into two stable dynamical states. The next phase of this study is to repeat the analysis using soliton simulations that are representative of these stable dynamical states. The final phase of the study will be generating the solitons in the shallower part of the Yellow Sea where it is believed that Zhou et al. [1] made their signal measurements. To firmly establish that solitons were responsible for the signal losses observed by Zhou et al., we will have to show that all three soliton states in the shallower region of the Yellow Sea are capable of producing acoustic signal losses. The work presented here is an important first step.

Acknowledgements

This work was funded by the Office of Naval Research under PE 602435N, with technical management provided by the Naval Research Laboratory. A grant of computer time from the Department of Defense's High Performance Computing program, and the use of the supercomputer facilities at the Major Shared

Resource Center, NAVO, Stennis Space Center, MS, are also acknowledged. This document is approved for public release.

Appendix A

The Lamb model [12] is based on the two-dimensional invisid incompressible Boussinesq equations on a rotating f plane:

$$\frac{\partial \vec{U}}{\partial t} + (\vec{U} \cdot \vec{\nabla})\vec{U} - fv\vec{i} = -\vec{\nabla} p - \rho \vec{g}$$

$$\frac{\partial v}{\partial t} + (\vec{U} \cdot \vec{\nabla})v + fu = 0$$

$$\frac{\partial \rho}{\partial t} + \vec{U} \cdot \vec{\nabla}\rho = 0$$

$$\vec{\nabla} \cdot \vec{U} = 0$$

$\vec{U} = (u, w)$ is the velocity vector in the cross-bank plane with (u, w) designating the horizontal and vertical velocities, respectively, and (x, z) designating the corresponding horizontal and vertical spatial coordinates, respectively; ρ the density; p the pressure; $\vec{g}$ the acceleration of gravity vector; f the Coriolis parameter. The gradient operator is given by $\nabla = \partial/\partial x + \partial/\partial z$, and t the time.

The along-bank direction is defined as perpendicular to the cross-bank direction. In the along-bank direction, $\vec{i}$ is the unit vector, the velocity is designated by, v, and the spatial coordinate by, y. While v is included in the model, $\partial v/\partial y$ is not allowed; hence, the characterization of the Lamb model as a 2.5-dimensional model.

The equations are transformed to a terrain following coordinate system (sigma-coordinates) which gives higher vertical resolution over the bank region. The equations are solved over a domain bounded below by the topography and above by a rigid surface. Fluid flow is forced by specifying the semi-diurnal tidal velocity on the left boundary. An absorption layer is also used to minimize computational boundary reflections. The right boundary is moved far to the right and a vertical pressure gradient is specified together with another absorption layer.

Appendix B

Starting with the Helmholtz equation for pressure, $\nabla^2 P(\vec{r}) + k^2 P(\vec{r}) = 0$, where the acoustic wave number, frequency, and sound speed are related by, $k(\vec{r}) = 2\pi f/C(\vec{r})$, and $\vec{r}$ is a three-dimensional spatial vector, write the operator, ∇^2, in cylindrical coordinates and assume azimuthal symmetry (for the ocean environment, this is a reasonable assumption). The Helmholtz equation is now of the form

$$\frac{\partial^2 P(r, z)}{\partial r^2} + \frac{1}{r}\frac{\partial P(r, z)}{\partial r} + \frac{\partial^2 P(r, z)}{\partial z^2} + k_0^2 n^2(r, z) P(r, z) = 0$$

The wavenumber is written in terms of the index of refraction of the ocean environment, n (r, z), as $k(r, z) = k_0 n(r, z)$, where a reference wavenumber, k_0, and sound speed, C_0, have been define, such that $k_0 = 2\pi f/C_0$.

The complex pressure field, $P(r, z)$, can be written in terms of a "reduced complex pressure field," $p(r, z)$, as $P(r, z) = p(r, z)/\sqrt{r}$. The cylindrical spreading term is removed, giving a reduced complex pressure equation:

$$\frac{\partial^2 p(r,z)}{\partial r^2} = -\left(k_0^2 n^2(r,z) + \frac{\partial^2}{\partial z^2}\right) p(r,z)$$

This equation can be factored into

$$\left[\frac{\partial}{\partial r} + ik_0\sqrt{(1+X)}\right]\left[\frac{\partial}{\partial r} - ik_0\sqrt{(1+X)}\right] p = 0$$

using the notation, $X = k_0^{-2}(\partial^2/\partial z^2 + k^2 - k_0^2)$, we obtain

$$\frac{\partial p}{\partial r} = ik_0\sqrt{(1+X)}\,p$$

This represents the outgoing (propagating) acoustic pressure field. The other factored equation represents the incoming acoustic energy (i.e. the backscattered fields). Causality requirements eliminates the incoming equation. One final step is to remove a common phase term, $\exp(ik_0 r)$. The one-way parabolic equation (PE) approximation now has the form

$$\frac{\partial p}{\partial r} = ik_0(-1 + \sqrt{(1+X)})\,p$$

The pseudo-differential operator term can be approximated by a Pade approximation, $-1+\sqrt{(1+X)} \cong \sum_{j=1}^{n} a_{j,n}X/(1 + b_{j,n}X)$, so that the outgoing pressure field can be found from,

$$\frac{\partial p}{\partial r} = ik_0 \sum_{j=1}^{n} \frac{a_{j,n}X}{1 + b_{j,n}X}\,p$$

By keeping a sufficient number of terms in the Pade approximation, high levels of accuracy can be obtained for the complex pressure field. The FEPE ocean acoustic model is based on this PE approximation. A decade of benchmarking has established that the FEPE model can accurately propagate acoustic energy throughout the ocean environment. This includes ocean environments that have multiple interactions with the rough ocean boundaries (e.g. sea surfaces, seafloors) and the fluctuating ocean volume (e.g. internal waves).

References

[1] J.X. Zhou, X.Z. Zhang, P.H. Rogers, Resonant interaction of sound wave with internal solitons in the coastal zone, J. Acoust. Soc. Am. 90 (1991) 2042–2054.

[2] S.A. Chin-Bing, D.B. King, J.E. Murphy, Numerical Simulations of lower-frequency acoustic propagation and backscatter from solitary internal waves in a shallow water environment, in: D.D. Ellis, J.R. Preston, H.G. Urban (Eds.), Ocean Reverberation, Kluwer Academic Publishers, The Netherlands, 1993.

[3] S.A. Chin-Bing, D.B. King, R.W. McGirr, Computer modelling of time-domain and frequency-domain acoustic signals in a shallow-water ocean environment with internal waves, Math. Model. Scientific Comput. 4 (1994) 377–385.

[4] D.B. King, S.A. Chin-Bing, R.W. McGirr, Effect of shallow water internal waves on broadband acoustic wave propagation, in: D. Lee, M. Shultz (Eds.), Theoretical and Computational Acoustics: Environmental Acoustics, vol. 2, World Scientific, Singapore, 1994, pp. 793–807.
[5] R.H. Headrick Jr, J.F. Lynch, M. Orr, B. Pasewark, S. Wolf, M. Badiey, C.-S. Chiu, J. Apel, Acoustic travel time and intensity fluctuations measured in the SWARM95 experiment. Part 2, J. Acoust. Soc. Am. 102 (5) (1997) 3016.
[6] D. Tielburger, S. Finette, S. Wolf, Acoustic propagation through an internal wave field in a shallow water wave guide, J. Acoust. Soc. Am. 101 (1997) 879–880.
[7] J.C. Preisig, T.F. Duda, Coupled acoustic mode propagation through continental shelf internal solitary waves, IEEE J. Oceanic Eng. 22 (1997) 256–269.
[8] A.C. Warn-Varnas, S.A. Chin-Bing, D.B. King, S.A. Piacsek, A. MacNaughton, Modeling the effects of solitons on acoustics, in: Proceedings of Workshop on Internal Solitary Waves in the Ocean: Their Physics and Implications for Acoustics, Biology, and Geology, Victoria, BC, Canada, 27–29 October 1998.
[9] S.A. Chin-Bing, D.B. King, A. Warn Varnas, On the anomalous resonance effect caused by shallow water solitons. Part 2, J. Acoust. Soc. Am. 102 (5) (1997) 3215.
[10] A. Warn-Varnas, S.A. Chin-Bing, D.B. King, Z. Hallock, Ocean–acoustic soliton studies and predictions, Surv. Geophys., submitted for publication.
[11] S.A. Chin-Bing, D.B. King, R.A. Zingarelli, A Search Algorithm for Resonance Anomalies (SARA), The 1999 NRL Review, Naval Research Laboratory, 1999, pp. 71–72.
[12] K. Lamb, Numerical experiments of internal wave generation by strong tidal flow across a finite amplitude bank edge, J. Geophys. Res. 99 (1994) 848–864.
[13] M.D. Collins, Higher-order, energy-conserving, two-way, and elastic parabolic equations, in: S.A. Chin-Bing, D.B. King, J.A. Davis, R.B. Evans (Eds.), Proceedings of the Second Parabolic Equation Workshop (PE Workshop II), Naval Research Laboratory, Stennis Space Center, MS, NRL/BE/7181-93-0001, 1993, pp. 145–168.
[14] M.D. Collins, A higher-order parabolic equation for wave propagation in an ocean overlying an elastic bottom, J. Acoust. Soc. Am. 86 (1989) 1459–1464.
[15] M.D. Collins, FEPE user's guide, NRL (NORDA) TN-365, Naval Research Laboratory, Stennis Space Center, MS, USA, 1988.
[16] M.D. Collins, E.K. Westwood, A higher-order energy-conserving parabolic equation for range-dependent ocean depth, sound speed, and density, J. Acoust. Soc. Am. 89 (1991) 1068–1075.